

# Morphology and Magnetic Properties of Hollow $\text{Co}_3\text{O}_4$ Spheres

A. V. Dmitriev<sup>a</sup>, E. V. Vladimirova<sup>a,\*</sup>, A. P. Esaulkov<sup>a</sup>, V. D. Zhuravlev<sup>a</sup>,  
M. V. Kuznetsov<sup>a</sup>, and S. A. Uporov<sup>b</sup>

<sup>a</sup> Institute of Solid State Chemistry, Ural Branch, Russian Academy of Sciences, Yekaterinburg, Russia

<sup>b</sup> Institute of Metallurgy, Ural Branch, Russian Academy of Sciences, Yekaterinburg, Russia

\*e-mail: vladimirova@ihim.uran.ru

Received August 20, 2020; revised August 20, 2020; accepted August 26, 2020

**Abstract**—Nanostructured hollow  $\text{Co}_3\text{O}_4$  spheres are synthesized by ultrasonic spray pyrolysis. Nanocrystals forming the sphere structure have different sizes and packing density, depending on the synthesis conditions. The samples are studied by X-ray diffraction, scanning electron microscopy, low-temperature nitrogen adsorption, vacuum pycnometry, and Raman and X-ray photoelectron spectroscopies. The field and temperature dependences of magnetization show that the magnetic properties and the Néel temperature of  $\text{Co}_3\text{O}_4$  hollow spheres are determined by the size and packing density of nanocrystals.

**Keywords:** ultrasound spray pyrolysis, hollow  $\text{Co}_3\text{O}_4$  spheres, weak ferromagnetism, exchange bias, Néel temperature

**DOI:** 10.1134/S1063783420120082

## 1. INTRODUCTION

Nanostructured magnetic materials are of interest from the perspective of both fundamental science and various applications such as spintronics, magneto-optical devices, biomedicine, high-density data storage, to name a few [1, 2]. As of today, magnetic nanostructures have been prepared in the form of nanospheres [3], nanoboxes [4], nanorings [5], nanowires/rods/tubes [6], and thin films [7]. The magnetic properties of nanostructured materials are determined by the shape, size, and spatial arrangement of nanoparticles.

Hollow spheres are of interest due to their low density and large pore volume; they may find use in medical diagnostics and for controlled drug release [8, 9], energy accumulation and storage [10, 11], photocatalysis [11, 12], and chemical sensors [13, 14]. The cobalt oxide  $\text{Co}_3\text{O}_4$  may be a promising material for such applications. Bulk  $\text{Co}_3\text{O}_4$  is an antiferromagnetic material (AFM) with the Néel temperature  $T_N$  below 40 K [15, 16]. Magnetic moments in  $\text{Co}_3\text{O}_4$  arise due to  $\text{Co}^{2+}$  ions, mainly because of spins with a relatively small contribution of spin-orbit coupling [17].  $\text{Co}^{3+}$  ions in octahedral positions are diamagnetic because of splitting of the  $3d$ -levels by the octahedral crystal field and complete filling of  $t_{2g}$  levels. Studies of  $\text{Co}_3\text{O}_4$  nanoparticles showed that metastable states, such as superparamagnetic and spin glass states [17–19], result from increases in the nanocrystal surface area. It was found [20] that  $\text{Co}_3\text{O}_4$  nanoparticles dispersed in

$\text{SiO}_2$  exhibited superparamagnetic behavior with blocking temperature  $T_B = 3.4$  K. In particles with a size of 17 nm, an antiferromagnetic transition was detected at 26 K, whereas for bulk samples with a size of 1–2  $\mu\text{m}$  such a transition was observed at 30 K [21]. Additionally, weak ferromagnetism (FM) and the exchange-bias effect were detected below the Néel temperature [21]. Mousavand et al. [22] established the dependence of  $T_N$  on the number of particles in  $\text{Co}_3\text{O}_4$  and observed an increase in magnetization at temperature  $T_f = 10$  K [22], which was related to the interaction between uncompensated moments at the crystal surface.

Considerably fewer works have been published on the magnetic properties of nanostructured materials. The nature of such materials is determined not only by the properties of nanoparticles, but also the interaction between them. Systems of interacting magnetic nanoparticles can exhibit a plethora of different phenomena that are interesting from scientific and applied perspectives [23].

The magnetic properties of hollow  $\text{Co}_3\text{O}_4$  spheres were discussed in [24]. The enhancement in their ferromagnetic properties (coercive force and magnetization), as related to a decrease in the sphere diameter, was explained by an increase in the surface curvature. We think that the magnetic properties are determined not only by the sphere diameter but also by their morphology (i.e., the particle size and their packing density in the shell). So far, the effect of these factors on

magnetic properties of hollow  $\text{Co}_3\text{O}_4$  spheres have not been investigated.

Self-assembly is a means of bringing nanostructured materials to different morphologies. In particular, self-assembly is observed upon evaporation of the solvent from a precursor solution. With competition between the rate of evaporation and diffusion of dissolved components, a random distribution of dissolved particles is changed for a distribution with a certain, fixed morphology. Among different synthesis techniques, ultrasonic spray pyrolysis (USP) represents a simple and versatile approach enabling control over self-assembly of hollow spheres from solutions. By varying the rate of solvent removal (by adjusting the evaporation temperature of aerosol drops) and the diffusion rate of dissolved components (due to formation of organometallic complexes), spheres with different morphologies can be prepared [25–27].

The aim of this work is to synthesize hollow  $\text{Co}_3\text{O}_4$  spheres with different shell densities by USP and establish the effects that the nanoparticle size and packing density have on their magnetic properties.

## 2. EXPERIMENTAL

$\text{Co}_3\text{O}_4$  was synthesized using a 1.75 M cobalt nitrate solution. A USP unit with an ultrasound frequency of 1.7 MHz was employed in synthesis [28]. Aerosol mixed into a stream of air flowing at a rate of 14.6 mL/s was supplied into a tubular furnace consisting of two parts: one for drying aerosol drops and another for synthesis. After the synthesis stage was complete, the powder was captured by an electrostatic filter. Three samples were synthesized: sample 1 was obtained using the nitrate solution, and the evaporation temperature was 623 K; sample 2 was obtained using the nitrate solution, and the evaporation temperature was 723 K; and sample 3 was obtained using the nitrate solution with an addition of 2 moles of tartaric acid per 1 mole of  $\text{Co}_3\text{O}_4$ , and the evaporation temperature was 623 K. The synthesis temperature for all three samples was 1173 K.

The phase analysis was performed on an XRD-7000 (Shimadzu) diffractometer equipped with a secondary monochromator using  $\text{CuK}_\alpha$  radiation and scanning over the  $2\theta$  range of  $20^\circ$  to  $80^\circ$  at a step size of  $0.03^\circ$ . X-ray diffraction (XRD) studies were performed on an automatic STOE STADI-P diffractometer equipped with a linear mini-PSD detector using  $\text{CuK}_\alpha$  radiation and scanning over the  $2\theta$  range of  $5^\circ$  to  $120^\circ$  at a step size of  $0.02^\circ$ . Polycrystalline silicon was used as an external standard ( $a = 5.43075(5) \text{ \AA}$ ). The morphology of prepared spheres was studied using a JEOL 6390 LA scanning electron microscope (SEM). The porous structure of samples was studied by low-temperature (77 K) nitrogen adsorption on a Gemini VII and Porosity 2390t surface area analyzer (Micro-

metrics). The porosity parameters were evaluated by the Brunauer–Emmett–Teller (BET) and Barrett–Joyner–Halenda (BJH) methods. Density measurements were carried out on an AccuPyc II 1340 vacuum pycnometry system (Micrometrics, the United States). X-ray photoelectron spectroscopy (XPS) studies were carried out on a VG ESCALAB MK II spectrometer.  $\text{MgK}_\alpha$  radiation (1253.6 eV) was used as an X-ray excitation radiation, with a monochromator not being employed. The magnetic properties were studied on a VSM-5T cryogenic magnetometer capable of measuring in the range of field strength of  $\pm 50$  kOe and in the temperature range of 4–300 K. Raman spectroscopy measurements were performed on an InVia Reflex confocal dispersion Raman spectrometer (Renishaw, UK) equipped with a Leica DML confocal microscope, and a Nd : YAG laser ( $\lambda = 533 \text{ nm}$ ) was used as an excitation source.

## 3. RESULTS AND DISCUSSION

The XRD analysis showed that our  $\text{Co}_3\text{O}_4$  samples were single-phase samples with a spinel structure (space group  $Fd3m$ ). XRD patterns of all our samples are identical to that shown in Fig. 1, which is for sample 1. The unit cell parameter ( $a = 8.077(3) \text{ \AA}$ ) was found to be independent of the synthesis conditions and was similar to the value for corresponding bulk material [ICDD card 78-1969]. The coherent scattering region (CSR) size was determined by the Le Bail method using the Klug and Alexander approach [29], which enabled us to estimate the contribution of size effects to the value of full width at half-maximum (FWHM). The values for CSR were used to estimate the size  $d$  of particles constituting the spheres (Table 1). We note that a decrease in the crystallite size often leads to an increase in the lattice parameter value [30]. In our case, it nearly matches the value for bulk  $\text{Co}_3\text{O}_4$ . For nanoparticles smaller than 80 nm, the lattice parameter increases to  $8.1 \text{ \AA}$  [30]. To prepare nanoparticles of desired size, it is typical to vary the annealing temperature in the range of 723–1073 K, and the higher the annealing temperature the larger the  $\text{Co}_3\text{O}_4$  grain size. Nanoparticles synthesized at a temperature below 1073 K may have oxygen vacancies, which will result in larger values for lattice parameters. Our samples were synthesized at 1173 K. The fact that the lattice parameters did not change may be an indirect proof that their stoichiometric composition did not change either. SEM studies of the prepared powders showed that all our samples consist of agglomerates with a spherical shape and an average diameter of 1.15–1.30  $\mu\text{m}$  (Fig. 2 and Table 1). The experimentally measured density  $\rho_p$  of the samples was found to vary the range of  $5.42 \pm 0.02$  to  $6.06 \pm 0.02 \text{ g/cm}^3$  (Table 1). As can be seen, the density value for sample 1 is considerably smaller than the values calculated from XRD data ( $\rho_{XR} = 6.073 \text{ g/cm}^3$ ).

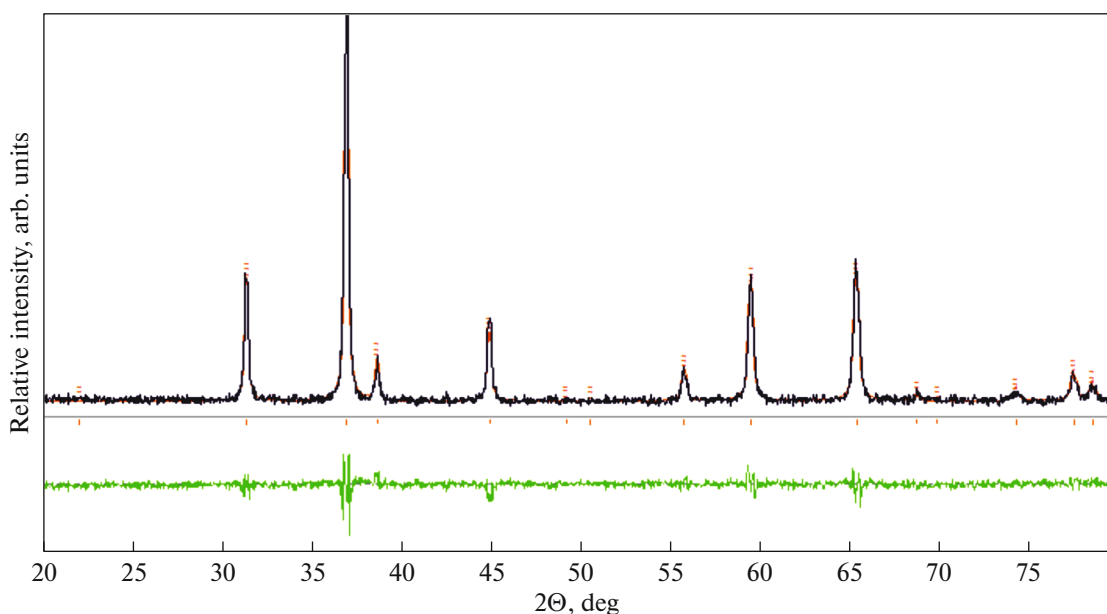


Fig. 1. Experimental, theoretical, and difference XRD patterns for  $\text{Co}_3\text{O}_4$  sample, sample 1.

To establish whether the prepared spheres were hollow, we measured the density of samples and estimated the average diameter of  $\text{Co}_3\text{O}_4$  spheres. The average diameter of spheres with density  $\rho_p$  can be estimated by using the mass conservation law in the form  $D_{\text{cal}} = d_{\text{drop}}(C/\rho_p)^{1/3}$ , where  $C$  is the solution concentration. The size of aerosol drops can be determined from the expression  $d_{\text{drop}} = 0.34(\pi\sigma/\rho_L f^2)^{1/3}$ , where  $\sigma$  is the solution surface tension (N/m),  $\rho_L$  is the solution density ( $\text{kg}/\text{m}^3$ ), and  $f$  is the ultrasound frequency (MHz) [31]. The experimentally measured density and surface tension of nitrate solution were  $1231 \text{ kg}/\text{m}^3$  and  $0.063 \text{ N}/\text{m}$ , respectively. The addition of tartaric acid resulted in an increase in the density and the solution surface tension to  $1365 \text{ kg}/\text{m}^3$  and  $0.068 \text{ N}/\text{m}$ , respectively. These measurements allowed us to calculate the average size of aerosol drops, which was  $2.50 \text{ }\mu\text{m}$  for the nitrate solutions and  $2.47 \text{ }\mu\text{m}$  for the solution containing tartaric acid, and the diameter of synthesized spheres, which was  $0.64$  and  $0.62 \text{ }\mu\text{m}$ , respectively. Experimentally measured average values for sphere diameter ( $1.15$ – $1.30 \text{ }\mu\text{m}$ ) were twice as high as the corresponding calculated values. This fact tells us that the synthesized samples con-

sist of hollow spheres, and the experimentally measured density represents the density of the shell rather than the whole sphere.

Additional information about the morphology of shells of hollow spheres was obtained from adsorption measurements. The registered adsorption/desorption isotherms for all samples were identified as type II isotherms according to the IUPAC classification, which correspond to nonporous or macroporous adsorbents with a pore size on the order of  $50 \text{ nm}$ . The experimental data on adsorption measurements summarized in Table 1 suggest that the volume of open pores and the specific surface area of samples increased as a result of increasing the evaporation temperature and adding tartaric acid. Considering the results of density measurements, we can conclude that closed pores rich the surface and the shell of hollow spheres becomes denser in the order from sample 1 to sample 3.

Confocal Raman spectroscopy was used to investigate the size effect in the phonon interaction between cobalt cations in nanoparticles constituting hollow  $\text{Co}_3\text{O}_4$  spheres. Raman spectra are shown in Fig. 3. All samples feature five key phonon excitations ( $F_{2g}^3 + E_g + F_{2g}^2 + F_{2g}^1 + A_{1g}$ ), which are in good agreement

Table 1. Summary of structural and magnetic measurements

Sample	$d$ , nm	$D$ , $\mu\text{m}$	$\rho_p$ , $\text{g}/\text{cm}^3$	$S$ , $\text{m}^2/\text{g}$	$V_p$ , $\text{cm}^3/\text{g}$	$T_p$ , K	$T_f$ , K	$T_{\text{irr}}$ , K	$H_c$ , T	$H_E$ , T
1	49.6	1.15	5.479	5.080	0.046	32	10	70	0.010	0.010
2	55.2	1.30	5.689	6.003	0.042	36	10	60	0.015	0.015
3	47.6	1.30	6.073	12.93	0.071	38	10	—	0	0

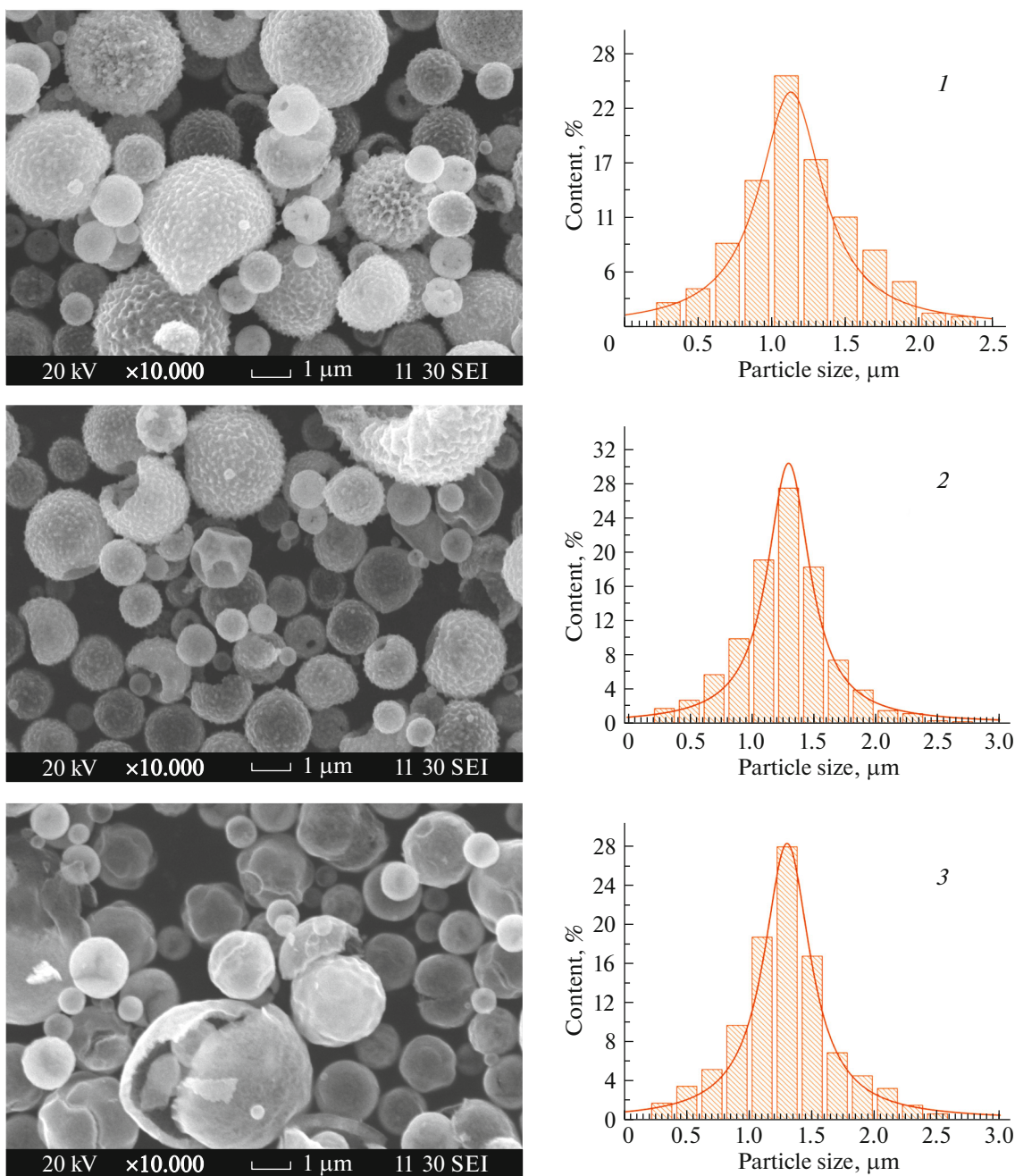


**Fig. 2.**  $\text{Co}_3\text{O}_4$  samples: SEM images and histograms of size distribution of spherical agglomerates: (1) sample 1, (2) sample 2, and (3) sample 3.

with values predicted by the group theory and are in line with literature data [30–32]. A band around  $680\text{ cm}^{-1}$  is considered to be a symmetrical stretching vibration of Co–O within the octahedral group ( $\text{CoO}_6$ ), which is assigned to  $A_{1g}$  vibration mode in the  $Oh7$  spectroscopic symmetry. Raman bands with an average intensity in the range of  $440\text{--}550\text{ cm}^{-1}$  have  $E_g$  and  $F_{2g}^2$  symmetries, respectively, whereas the weak zone near  $600\text{ cm}^{-1}$  has the  $F_{2g}^1$  symmetry. A band near

$190\text{ cm}^{-1}$  is characteristic of tetrahedral  $\text{CoO}_4$  nodes with the  $F_{2g}^3$  symmetry. This finding corroborates the formation of  $\text{Co}_3\text{O}_4$  nanocrystals. By comparing the Raman spectrum for sample 1 to that for sample 2, we can see that the increase in evaporation temperature leads to the corresponding bands narrowing and also shifting toward higher frequencies. Such changes in Raman spectra are typical of nanocrystals. For sample 1, the nanocrystal size is  $49\text{ nm}$ , and the  $A_{1g}$  and  $F_{2g}^2$

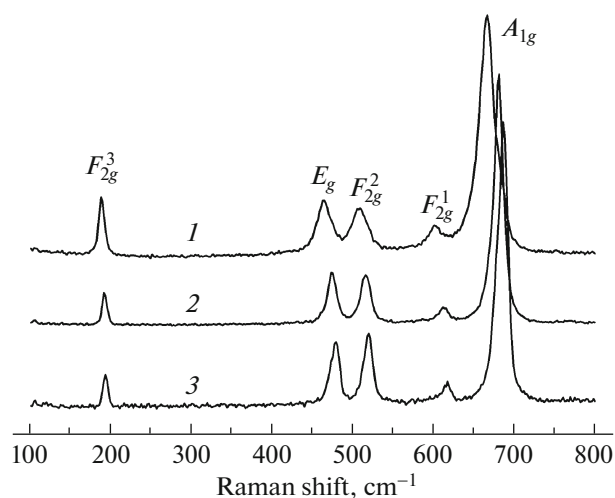


**Fig. 3.** Raman spectra of  $\text{Co}_3\text{O}_4$  samples: (1) sample 1, (2) sample 2, and (3) sample 3.

peaks occur at  $666.6$  and  $180\text{ cm}^{-1}$ , respectively; for sample 2, it is  $55\text{ nm}$ , and the  $A_{1g}$  and  $F_{2g}$  peaks occur at  $680$  and  $192\text{ cm}^{-1}$ , respectively, which is similar to findings reported in [30]. Substantial differences were seen in the spectrum for sample 3: the  $A_{1g}$  and  $F_{2g}$  peaks occur at  $685$  and  $193\text{ cm}^{-1}$ , respectively. Despite the fact that spheres comprised smaller nanocrystals ( $46\text{ nm}$ ), the Raman spectrum features narrow bands and their peaks approach those characteristic of the bulk material ( $A_{1g}$  at  $691\text{ cm}^{-1}$ ). Raman spectra of  $\text{Co}_3\text{O}_4$  nanoparticles with a diameter of  $30\text{ nm}$  were noted to strongly depend on the nanoparticle agglomeration state and the effects related to laser-induced heating [32]. In this part of the work, we can conclude that the sphere shell structure of sample 3 is considerably different from that of samples 1 and 2. The fact that the positions of Raman peaks in question are narrow and close to those registered for bulk  $\text{Co}_3\text{O}_4$  suggests sample 3 has a higher packing density than samples 1 and 2.

Using tartaric acid may presumably result in partial reduction of the cobalt oxide at the nanoparticle surface. To determine the chemical composition of nanoparticles constituting the surface of  $\text{Co}_3\text{O}_4$  spheres, we carried out an XPS study. With this method, the precision in numerical values for  $\text{Co}^{3+}$  and  $\text{Co}^{2+}$  cannot be better than  $20\%$  [33]; nevertheless, variation of the  $\text{Co}^{3+}/\text{Co}^{2+}$  ratio results in notable distortion of  $\text{Co } 2p$  spectra because of the structure of satellites [34]. The  $\text{Co } 2p$  and  $\text{O } 1s$  XPS spectra for samples 1–3 were totally identical (Fig. 4). The  $\text{Co } 2p$  spectrum features two lines—at  $780.0$  and  $795.2\text{ eV}$ —that correspond to  $2p_{3/2}$  and  $2p_{1/2}$  states with a spin-orbit splitting of  $15.2\text{ eV}$  and peaks related to satellites, which is in line with literature data [33]. In the oxygen  $\text{O } 1s$  peak, the key line with a binding energy of

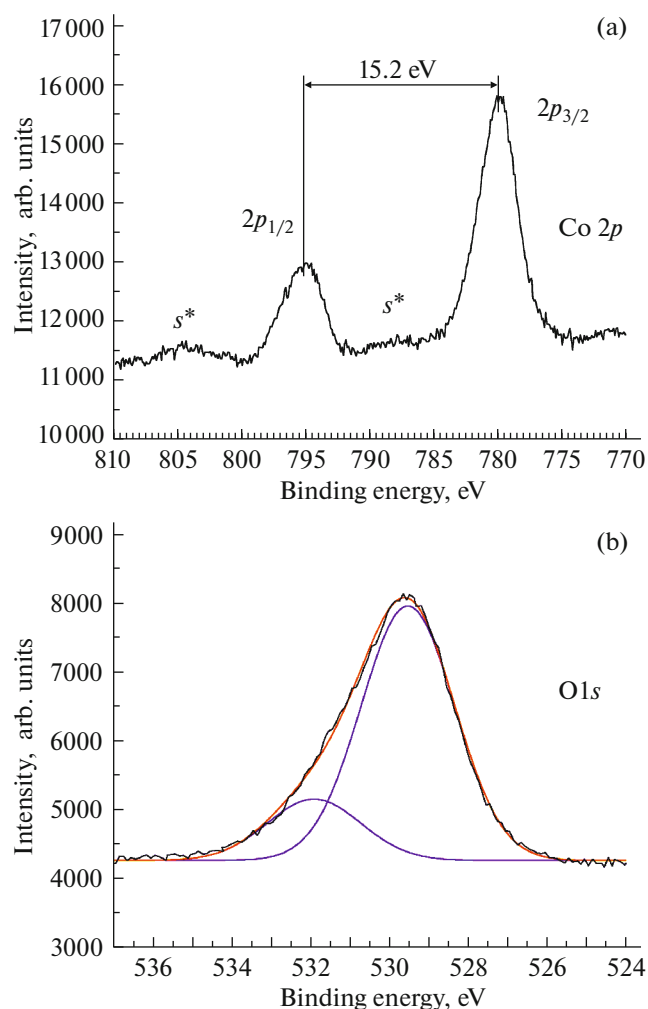


**Fig. 4.** XPS spectra for sample 1: (a)  $\text{Co } 2p$  and (b)  $\text{O } 1s$ .

$529.6\text{ eV}$  is related to oxygen in the  $\text{Co}_3\text{O}_4$  lattice [33], and a maximum at  $531.8\text{ eV}$  is related to adsorbed  $\text{OH}^-$  groups [34].

XPS analyses showed that all our samples have a totally identical surface chemical composition that corresponds to the  $\text{Co}_3\text{O}_4$  stoichiometry.

Thus, the synthesized samples are identical in terms of their surface and bulk chemical compositions and characterized by similar values for the average sphere diameter, which is  $1.1\text{--}1.3\text{ }\mu\text{m}$ . With our findings, the effects that nonstoichiometry and the curvature of sphere surface may have on the magnetic properties can be eliminated. At the same time, samples 1–3 differ in the particle size and particle packing density within the spherical shells. We anticipate that the differences in the nanoparticle size and packing density will have an effect on the magnetic properties of hollow  $\text{Co}_3\text{O}_4$  spheres.

At room temperature, the field dependences of magnetization were identical for the three considered



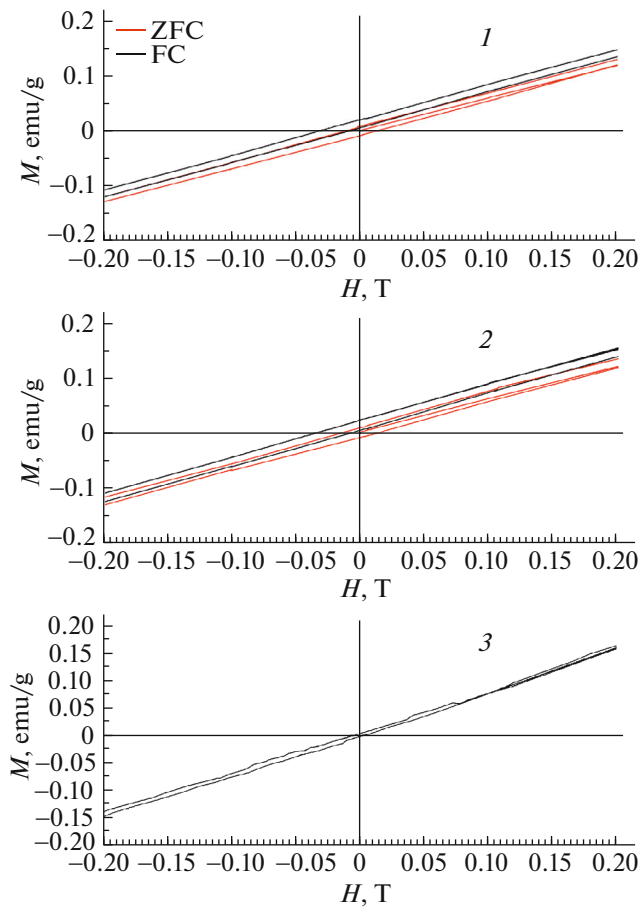


**Fig. 5.** Field dependences of magnetization registered at 4 K in the ZFC and FC modes at a field of 5 T for synthesized  $\text{Co}_3\text{O}_4$  samples: (1) sample 1, (2) sample 2, and (3) sample 3.

samples and corresponded to a paramagnetic state with zero coercivity ( $H_c$ ) and remanence ( $M_r$ ), which coincides with findings reported in [30]. The magnetization of considered hollow spheres in a field of 5 T at 4 K was 3.5 emu/g. This result is in line with literature data for  $\text{Co}_3\text{O}_4$  spheres with a diameter of 360 nm [24], albeit the diameter of our spheres is almost three times as much. The presence of weak ferromagnetism characterized by a remanence of 0.01 emu/g was found in samples 1 and 2, while their coercivity  $H_c$  was 0.01 and 0.015 T, respectively.

In the introduction, we remarked on the emergence of weak ferromagnetism in  $\text{Co}_3\text{O}_4$  nanopowders that was related to uncompensated spins at the surface. These particles can be considered as consisting of an AFM core and a FM shell. With this magnetic structure, a shift in the magnetic hysteresis loop occurs (exchange bias  $H_E$ ) [35]. Figure 5 shows the central parts of hysteresis loops measured in the zero field-cooling (ZFC) and field-cooling (FC) modes. In the ZFC mode, a sample was cooled in the zero field to a

temperature of 4 K, and the magnetization was measured at the magnetic fields spanning  $\pm 5$  T. In the FC mode, samples were cooled from room temperature to a temperature of 4 K while applying a field of 5 T, and their magnetization was measured at the magnetic fields spanning  $\pm 5$  T. As can be seen, the FC hysteresis loops for samples 1 and 2 shift toward the negative field and positive magnetization, whereas in the ZFC mode the loop remains centered around the axis origin. A shift in the FC loop is typically related to the exchange-bias effect. The coercive field and the exchange-bias field are defined by expressions  $H_c = (H_c^+ - H_c^-)/2$  and  $H_E = (H_c^+ + H_c^-)/2$ , respectively, where  $H_c^+$  ( $H_c^-$ ) is the positive (negative) coercive field (Fig. 5). The results of measurements are summarized in Table 1.

Typically, for noninteracting particles, the exchange bias increases with decreasing the particle diameter [30, 35]. In our case, this relationship does not hold. The  $H_E$  value for sample 1, which consists of smaller nanoparticles, is smaller than that for sample 2 which consists of larger particles. We note that the exchange bias is determined not only by the particle size but it also depends on such factors as the AFM and FM domain structure and surface roughness [35]. The dependence of  $H_E$  and  $H_c$  on the thickness  $t_{\text{FM}}$  of surface FM layer, which in our case is represented by the interface between nanoparticles, is another effect that may be of importance in nanostructured systems. The shift in hysteresis loop is inversely proportional to the FM layer thickness:  $H_E \sim 1/t_{\text{FM}}$  [36]. An increase in the shell density may result in the interface between nanoparticles having a smaller thickness and lead to an increase in  $H_E$  and  $H_c$ . Weak ferromagnetism and the exchange-bias effect were observed in hollow spheres with diameters of 360 and 680 nm [24]. The increase in coercive force and exchange bias with decreasing the sphere diameter that was found in [24] was attributed to an increase in the surface curvature, but, unfortunately, no data on the size and packing density of nanoparticles in spherical shells were provided in the cited study. The possibility of the surface curvature having an effect cannot be eliminated in our case either. Nevertheless, we can state that this effect is negligible, because samples 2 and 3 have similar average diameters, but their magnetic properties are different.

In contrast to samples 1 and 2, the field dependence of magnetization for sample 3 at 4 K varies linearly with the applied field with zero coercive force and the remanence, and this is how the corresponding bulk material behaves below Néel temperature  $T_N$  [30]. Lack of ferromagnetism in sample 3 is suggestive of a small number of uncompensated magnetic moments within nanoparticle interfaces.

The temperature dependences of magnetization registered in the ZFC and FC modes supplied addi-

tional information on the structure and the antiferromagnetic transition temperature. In ZFC measurements, a sample was cooled from 300 to 2 K in zero magnetic field, and magnetization was registered on heating the system in a magnetic field of 100 Oe. In FC measurements, a sample was cooled from 300 K to 2 K in a magnetic field of 100 Oe, and magnetization was registered on heating the system while continuing to apply the same magnetic field. The temperature-dependent ZFC and FC magnetizations are shown in Fig. 6. All the samples feature maxima below 40 K. In many works concerned with studying the magnetic properties of  $\text{Co}_3\text{O}_4$ , temperature  $T_p$  at maxima on ZFC and FC curves is related to Néel temperature  $T_N$  (i.e., the transition into antiferromagnetic state). It was remarked [21] that although  $T_p$  is a few degrees higher than  $T_N$ , it nonetheless reflects changes in  $T_N$  related to changes in the nanocrystal size. A precise value for  $T_N$  can be obtained from thermal capacitance measurements. The peak temperature increases from 32 to 38 K in the order from sample 1 to 3 (Fig. 6).

In magnetic nanomaterial, the self-limiting size effect occurs as the particle diameter decreases, which causes the temperature of magnetic ordering to lower. For samples 1 and 2,  $T_p$  varies with the particle size in a characteristic manner (Table 1). Sample 3, which comprises smaller particles, has a high  $T_p$ : 38 K, a value coinciding with that for corresponding bulk material [37]. This fact suggests that temperature  $T_N$  depends not only on the nanocrystal size but also on their packing density in the shell.

The  $M(T)$  curves can be used to identify characteristic features of samples 1 and 2 that are not found in sample 3. The ZFC and FC curves diverge at temperature  $T_{\text{irr}} \sim 70$  and 60 K, respectively (Table 1). A similar behavior of the temperature-dependent magnetization was observed on several experimental ZFC and FC curves for  $\text{Co}_3\text{O}_4$  nanoparticles [17–22, 30]. The divergence of ZFC and FC curves can be attributed to the spin glass behavior of uncompensated spins at the nanocrystal surface. For sample 3, the  $M(T)$  dependences registered in ZFC and FC modes overlap completely, a characteristic feature of the bulk material [37].

For all the samples, magnetization increases at the temperature defined as freezing temperature  $T_f = 10$  K (Fig. 6). This temperature is related to the freezing of uncompensated surface spins. This relation was reported repeatedly for  $\text{Co}_3\text{O}_4$  nanoparticles with different sizes, while it was not observed in corresponding bulk samples. The increase in magnetization observed for sample 3 below 10 K is a feature that differentiates it from the bulk material. The presence of low-temperature transition suggests that uncompensated spins are present at the surface [38].

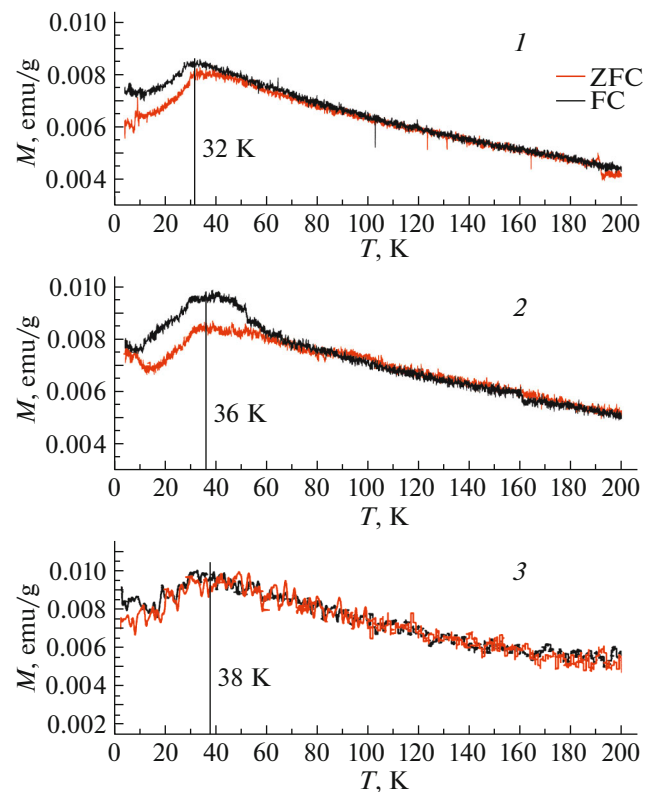


**Fig. 6.** ZFC and FC temperature-dependent magnetization of  $\text{Co}_3\text{O}_4$  samples registered at a field of 0.01 T: (1) sample 1, (2) sample 2, and (3) sample 3.

#### 4. CONCLUSIONS

By variation of the chemical composition and crystal structure, ultrasonic spray pyrolysis (USP) enabled us to create functional materials with unique properties that cannot be obtained by conventional methods of inorganic chemistry. The properties of such materials stem from the size of particles and the formation of interfaces between them. The material within interfaces is in a special amorphous state and often plays key part in determining the magnetic properties. Search for methods enabling control over interfaces may prove to be an effective means of obtaining materials with new practically important properties.

In this work, we used USP to synthesize hollow  $\text{Co}_3\text{O}_4$  spheres with identical lattice parameters and almost equal average sphere diameters. The size of nanocrystals constituting the hollow spheres and their packing density are the distinctive features. By studying the field and temperature dependences of magnetization of such samples, we established that the magnetic properties of hollow spheres are determined not only by the size of nanoparticles but their packing density as well. By varying the packing density, spheres with magnetic properties characteristic of both nanoparticles and the corresponding bulk material can be prepared.

## ACKNOWLEDGMENTS

XRD studies were carried out in the Laboratory of Structural and Phase Analysis, Institute of Solid State Chemistry, Ural Branch, Russian Academy of Sciences. The authors are grateful to E.S. Ul'yanova and M.V. Kandaurov for registering Raman spectra.

## FUNDING

The work was supported within a state assignment of scientific research in the Institute of Solid State Chemistry, Ural Branch, Russian Academy of Sciences (AAAA-A19-119031890026-6).

## CONFLICT OF INTEREST

The authors declare that they have no conflicts of interest.

## REFERENCES

1. D. Sellmyer and R. Skomski, *Advanced Magnetic Nanostructures* (Springer Science, New York, 2006).
2. S. D. Bader, *Rev. Mod. Phys.* **78**, 1 (2006).
3. J. I. Martín, J. Nogués, K. Liu, J. L. Vicent, and I. K. Schuller, *J. Magn. Magn. Mater.* **256**, 449 (2003).
4. T. He, D. R. Chen, X. L. Jiao, and Y. L. Wang, *Adv. Mater.* **18**, 1078 (2006).
5. M. Kläui, C. A. F. Vaz, L. Lopez-Diaz, and J. A. C. Bland, *J. Phys.: Condens. Matter* **15**, R985 (2003).
6. A. Fert and L. Piraux, *J. Magn. Magn. Mater.* **200**, 338 (1999).
7. Y. B. Xu and S. M. Thompson, *Spintronic Materials and Technology* (Taylor and Francis Group, London, UK, 2007).
8. V. Raman, S. Suresh, P. A. Savarimuthu, T. Raman, A. M. Tsasakis, K. S. Golokhvast, and V. K. Vadivel, *Exp. Therap. Med.* **11**, 553 (2015).
9. W.-Ch. Lin, Ch.-Ch. Chuang, Ch.-J. Chang, Y.-H. Chiu, M. Yan, and Ch.-M. Tang, *Nanomaterials* **9**, 200 (2019).
10. X. W. Lou, L. A. Archer, and Z. C. Yang, *Adv. Mater.* **20**, 3987 (2008).
11. M. K. Lima-Tenário, C. S. Ferreira, Q. H. F. Rebelo, R. F. B. de Souza, R. R. Passos, E. A. G. Pineda, and L. A. Pocrifka, *Mater. Res.* **21**, e20170521 (2018).
12. J. G. Yu, X. X. Yu, B. B. Huang, X. Y. Zhang, and Y. Dai, *Cryst. Growth Des.* **9**, 1474 (2009).
13. Z. L. Wu, K. Yu, S. D. Zhang, and Y. Xie, *J. Phys. Chem. C* **112**, 11307 (2008).
14. Y.-E. Chang, D.-Y. Youn, G. Ankonina, D.-J. Yang, H.-G. Kim, A. Rothschild, and I.-D. Kim, *Chem. Commun.*, 4019 (2009).
15. H. T. Zhu, J. Luo, J. K. Liang, G. H. Rao, J. B. Li, J. Y. Zhang, and Z. M. Du, *Phys. B: Condens. Matter* **403**, 3141 (2008).
16. B. Raveau and M. M. Seikh, in *Cobalt Oxides: From Crystal Chemistry to Physics* (Wiley, Weinheim, 2012), Chap. 5, p. 211.
17. Y. Hayakawa, S. Kohiki, M. Sato, Y. Sonda, T. Babasaki, H. Deguchi, A. Hidaka, H. Shimooka, and S. Takahashi, *Phys. E (Amsterdam, Neth.)* **9**, 250 (2001).
18. J. A. Mydosh, *Spin Glasses: An Experimental Introduction* (Taylor and Francis, London, 1993).
19. S. Sarkar, A. Mondal, N. Giri, and R. Ray, *Phys. Chem. Chem. Phys.* **21**, 260 (2019).
20. S. Takada, M. Fujii, and S. Kohiki, *Nanocryst. Nano Lett.* **1**, 379 (2001).
21. P. Dutta, M. S. Seehra, S. Thota, and J. Kumar, *J. Phys.: Condens. Matter* **20**, 015218 (2008).
22. T. Mousavand, T. Naka, K. Sato, S. Ohara, M. Umet-su, S. Takami, T. Nakane, A. Matsushita, and T. Adschiri, *Phys. Rev. B* **79**, 1 (2009).
23. S. V. Komogortsev, V. A. Fel'k, and O. A. Li, *J. Magn. Magn. Mater.* **473**, 410 (2019).
24. Q.-L. Ye, H. Yoshikawa, and K. Awaga, *Materials* **3**, 1244 (2010).
25. A. V. Dmitriev, E. V. Vladimirova, M. V. Kandaurov, D. G. Kellerman, A. Yu. Chufarov, and A. P. Tyutyunnik, *J. Alloys Compd.* **743**, 654 (2018).
26. A. V. Dmitriev, E. V. Vladimirova, M. V. Kandaurov, D. G. Kellerman, M. V. Kuznetsov, L. U. Buldakova, and R. F. Samigullina, *J. Alloys Compd.* **777**, 586 (2019).
27. A. V. Dmitriev, E. V. Vladimirova, M. V. Kandaurov, D. G. Kellerman, A. Yu. Chufarov, N. V. Tarkina, and A. P. Tyutyunnik, *J. Electr. Mater.* **48**, 4959 (2019).
28. A. V. Dmitriev, E. V. Vladimirova, M. V. Kandaurov, A. Yu. Chufarov, and D. G. Kellerman, *Phys. Solid State* **59**, 2360 (2017).
29. H. P. Klug and L. E. Alexander, *X-ray Diffraction Procedures for Polycrystalline and Amorphous Materials* (Wiley-Interscience, New York, 1974).
30. S. R. Gawali, A. C. Gandhi, S. S. Gaikwad, J. Pant, T.-S. Chan, C.-L. Cheng, and S. Y. Wu, *Sci. Rep.* **8**, 1 (2018).
31. R. J. Lang, *J. Acoust. Soc. Am.* **34**, 785 (1962).
32. I. Lorite, J. J. Romero, and J. F. Fernández, *J. Raman Spectrosc.* **43**, 1443 (2012).
33. D. Cabrera-German, G. Gomez-Sosa, and A. Herrera-Gomez, *Surf. Interface Anal.* **48**, 252 (2016).
34. Y. Xu, Z. Liu, D. Chen, Y. Song, and R. Wang, *Prog. Natl. Sci.: Mater. Int.* **27**, 197 (2017).
35. J. Nogués, J. Sort, V. Langlais, V. Skumryev, S. Surinach, J. S. Muñoz, and M. D. Baro, *J. Phys. Rep.* **422**, 65 (2005).
36. J. F. Bobo, L. Gabillet, and M. Bibes, *J. Phys.: Condens. Matter* **16**, S471 (2004).
37. S. Thota and S. Singh, in *Nature of Magnetic Ordering in Cobalt—Based Spinels, Magnetic Spinels—Synthesis, Properties and Applications*, Ed. by Mohindar Singh Seehra (Intech Open, Rijeka, 2017).
38. S. Sarkar, A. Mondal, N. Giri, and R. Ray, *Phys. Chem. Chem. Phys.* **21**, 260 (2019).

Translated by A. Kukharuk